AGU PUBLICATIONS

JGR

Journal of Geophysical Research: Atmospheres

RESEARCH ARTICLE
10.1002/2015JD023604

Key Points:
- First two-lidar study of 1 h mesoscale GW at two locations using CRRL lidars and temperature mapper
- Direct measurement of 1 h wave amplitudes in vertical wind and other components
- Method developed to fully characterize mesoscale GWs using coordinated instruments at multiple cites

Correspondence to:
X. Lu and X. Chu,
xian.lu@colorado.edu;
xinzhao.chu@colorado.edu

Citation:
Lu, X., C. Chen, W. Huang, J. A. Smith, X. Chu, T. Yuan, P.-D. Pautet, M. J. Taylor, J. Gong, and C. Y. Cullens (2015), A coordinated study of 1 h mesoscale gravity waves propagating from Logan to Boulder with CRRL Na Doppler lidars and temperature mapper, *J. Geophys. Res. Atmos.*, *120*, 10,006–10,021, doi:10.1002/2015JD023604.

Received 29 APR 2015
Accepted 7 SEP 2015
Accepted article online 11 SEP 2015
Published online 6 OCT 2015

A coordinated study of 1 h mesoscale gravity waves propagating from Logan to Boulder with CRRL Na Doppler lidars and temperature mapper

Xian Lu[1], Cao Chen[1,2], Wentao Huang[1], John A. Smith[1,2], Xinzhao Chu[1,2], Tao Yuan[3], Pierre-Dominique Pautet[3], Mike J. Taylor[3], Jie Gong[4], and Chihoko Y. Cullens[5]

[1]Cooperative Institute for Research in Environmental Sciences, University of Colorado Boulder, Boulder, Colorado, USA, [2]Department of Aerospace Engineering Sciences, University of Colorado Boulder, Boulder, Colorado, USA, [3]Center for Atmospheric and Space Sciences, Utah State University, Logan, Utah, USA, [4]Universities Space Research Association, NASA Goddard Space Flight Center, Greenbelt, Maryland, USA, [5]Space Science Laboratory, University of California, Berkeley, California, USA

Abstract We present the first coordinated study using two lidars at two separate locations to characterize a 1 h mesoscale gravity wave event in the mesopause region. The simultaneous observations were made with the Student Training and Atmospheric Research (STAR) Na Doppler lidar at Boulder, CO, and the Utah State University Na Doppler lidar and temperature mapper at Logan, UT, on 27 November 2013. The high precision possessed by the STAR lidar enabled these waves to be detected in vertical wind. The mean wave amplitudes are ~0.44 m/s in vertical wind and ~1% in relative temperature at altitudes of 82–107 km. Those in the zonal and meridional winds are 6.1 and 5.2 m/s averaged from 84 to 99 km. The horizontal and vertical wavelengths inferred from the mapper and lidars are ~219 ± 4 and 16.0 ± 0.3 km, respectively. The intrinsic period is ~1.3 h for the airglow layer, Doppler shifted by a mean wind of ~17 m/s. The wave packet propagates from Logan to Boulder with an azimuth angle of ~135° clockwise from north and an elevation angle of ~ 3° from the horizon. The observed phase difference between the two locations can be explained by the traveling time of the 1 h wave from Logan to Boulder, which is about ~2.4 h. The wave polarization relations are examined through the simultaneous quantifications of the three wind components and temperature. This study has developed a systematic methodology for fully characterizing mesoscale gravity waves, inspecting their intrinsic properties and validating the derivation of horizontal wave structures by applying multiple instruments from coordinated stations.

1. Introduction

Essentially generated by the buoyancy force, gravity waves (GWs) are ubiquitous in the Earth's atmosphere and have been attracting intensive research activities for decades due to their prominent role in atmosphere's energetics, dynamics, and chemistry [e.g., *Holton*, 1983; *Garcia and Solomon*, 1985; *Vincent and Alexander*, 2000; *Fritts and Alexander*, 2003; *Sato*, 1994; *Sato and Yoshiki*, 2008; *Gardner and Liu*, 2010]. Among them, mesoscale GWs, defined as waves with horizontal wavelengths of 50–500 km and periods of 1–4 h according to *Uccellini and Koch* [1987], have very important effects on weather systems by affecting mesoscale cloud and precipitation patterns [*Koch and O'Handly*, 1997; *Zhang*, 2004]. They play a more significant role in the transport of momentum to the mesosphere and lower thermosphere (MLT) region than the subsynoptic waves [*Fritts and Nastrom*, 1992] and affect ionospheric variability by seeding medium-scale traveling ionospheric disturbances [*Bertin et al.*, 1978; *Kubota et al.*, 2011; *Ding et al.*, 2011]. Physical and dynamical mechanisms capable of generating mesoscale GWs are largely related to lower atmosphere activities, such as convection, ageostrophic accelerations, shear instability, topographic forcing, geostrophic adjustment, and strong diabatic heating [*Hooke*, 1986; *Zhang*, 2004; *Alexander and Barnet*, 2007; *Plougonven and Zhang*, 2014]. Therefore, through the vertical propagation, the mesoscale GWs play important roles in delivering the impacts of the terrestrial weather to the space weather at higher altitudes.

Numerous techniques have been developed to detect and characterize GWs, but it has been extremely difficult to use a single technique to provide complete information of wave parameters. This is probably

because almost all techniques have their own limitations and suffer the problem of observational filtering as each of them is only sensitive to a certain portion of the wave spectra and can capture a certain part of the wave characteristics [*Gardner and Taylor*, 1998; *Alexander*, 1998; *Preusse et al.*, 2008; *McDonald et al.*, 2010; *McDonald*, 2012]. For example, airglow imagers are good at resolving horizontal scales especially for high-frequency GWs, but they lack the information of altitude range. Range-resolved measurements such as lidars and radars are superior in continuous temporal coverage and decent temporal and vertical resolution, but they cannot provide the horizontal information directly unless multiple stations are studied in conjunction. Compared to ground-based instruments, spaceborne observations surpass in their excellent global coverage but underperform in the relatively poor temporal and spatial resolution. Nevertheless, it is plausible that multiple techniques have certain common wave spectra that can be fully or marginally resolved, and under this situation one type of measurement becomes complementary to the other and a coordinated study becomes valuable.

Although relatively rare, the observations of mesoscale and medium-frequency GWs have been reported recently using multiple types of measurements in the MLT region. *Suzuki et al.* [2013] have reported a GW event with a horizontal wavelength of 277 km and a wave period of 59 min from a combination of the Na lidar and airglow imager observations at the Arctic Lidar Observatory for Middle Atmosphere Research (ALOMAR) station (69.3°N, 16.0°E). Using an Advanced Mesospheric Temperature Mapper (AMTM) and correlative instrumentation, *Fritts et al.* [2014] have identified a 1 h wave event with horizontal and vertical wavelengths of ~200 and ~20 km, respectively, and with an estimated momentum flux of ~60 m^2/s^2 at ALOMAR. Utilizing the simultaneous observations from the AMTM and a Na lidar at Utah State University (USU), *Cai et al.* [2014] have found that the superposition of mesoscale medium-frequency GWs and the tidal waves can induce transient dynamic instabilities and cause wave breaking. Measurements from a Fabry-Perot interferometer and an airglow imager have also captured an intense GW with a horizontal wavelength of 790 km and a period of 1.5 h near the mesopause region at Shigaraki, Japan [*Shiokawa et al.*, 2007]. *Suzuki et al.* [2013] used a ray tracing method and located the wave source to a distortion of the polar jet at the tropopause, while *Shiokawa et al.* [2007] conjectured the wave source by identifying a nearby well-developed low-pressure cell and a distortion of the jet stream.

Our study aims at combining the three ground-based instruments (two Na Doppler lidars and one airglow imager) for the first two-lidar coordinated study at two separate locations for a 1 h mesoscale GW event over the Central U.S. and providing a complete direct characterization of such waves in the MLT region. In addition to temperatures and horizontal winds, we provide the direct measurements of GW amplitudes in vertical winds. Although the vertical winds measured by resonance Doppler lidars [*Gardner et al.*, 1995; *Gardner and Yang*, 1998], incoherent scatter radars [*Hoppe and Fritts*, 1995; *Mitchell and Howells,* 1998], and medium-frequency (MF) radars [*Franke et al.*, 1990] have been used to study gravity waves and to derive the gravity wave-induced heat and constituent fluxes [*Liu and Gardner*, 2005; *Gardner and Liu,* 2007, 2010], high-precision vertical winds are still relatively rare in the full characterization of gravity wave events. Such a case study is important in laying a foundation for a following statistical study that uses multiple instruments to fully characterize the high-to-medium frequency and mesoscale GWs. As the high-resolution Whole Atmosphere Community Climate Model and Whole Atmosphere Model start to resolve mesoscale waves, the statistical study from observations will provide an important reference for the models. Numerous statistical studies have been performed previously and provided rich information about the wave characteristics even though most of them applied either the lidar data or the imager data [*Gardner et al.*, 1989; *Beatty et al.*, 1992; *Hu et al.*, 2002; *Pautet et al.*, 2005; *Li et al.*, 2011]. An advantage of combining these two data sets is that the three fundamental wave parameters, i.e., periods, horizontal, and vertical wavelengths, are all inferred from observations directly, instead of using two of the observed parameters to derive the third one. Without the knowledge of background winds, such derivation is usually based on a big assumption that the intrinsic wave frequency is equal to the ground-based frequency, which more than often is not true.

2. Coordinated Observations With CRRL Lidars and USU AMTM in the Central U.S.

This study was enabled by the coordinated observations with two Na Doppler lidars of the Consortium of Resonance and Rayleigh Lidars (CRRL) at Boulder, CO, and Logan, UT, in collaboration with an AMTM [*Pautet et al.*, 2014] located at Bear Lake Observatory (41.9°N, 111.4°W) nearby Logan, in the night of

27 November 2013, from ~1 to 13 UT. Under the CRRL umbrella, the Consortium Technology Center, hosted by the University of Colorado Boulder, operates a Student Training and Atmospheric Research (STAR) Na Doppler lidar from the Table Mountain Lidar Observatory (40.1°N, 105.2°W) north of Boulder [*Smith et al.*, 2012; *Huang et al.*, 2013], while the Utah State University (USU) lidar group operates a Na Doppler lidar from the USU campus in Logan (41.7°N, 111.8°W) [*Yuan et al.*, 2013].

Originally constructed by graduate students in summer 2010, this STAR lidar received several upgrades in the following years making it more powerful and sophisticated [*Smith et al.*, 2012]. In 2011, significant improvements of the receiver efficiency as described in *Smith and Chu* [2015] enabled this STAR lidar to obtain very high resolution data. In 2013 the dual acoustic-optic frequency shifters were upgraded from ±480 MHz to ±750 MHz, making the STAR lidar more sensitive for vertical wind, temperature, and Na density measurements. The USU lidar group inherited the Na Doppler lidar system developed at Colorado State University [*She and Krueger*, 2007]. It had been operating in Fort Collins, CO (41°N, 105°W), for nearly two decades since 1990 before its relocation to USU during the summer of 2010 for continuing exploration of the midlatitude mesopause region. The USU lidar is capable of measuring temperatures, horizontal winds, and Na densities in the mesopause region through full diurnal cycles under clear sky conditions [*Yuan et al.,* 2013, 2014].

The STAR lidar signal levels reached over 1000 counts per laser shot through the Na layers from 80 to 115 km with the averaged laser power of ~500 mW at 30 Hz repetition rate and a telescope primary mirror of ~80 cm in diameter. Through laboratory testing, the photon detectors and discriminators have been carefully calibrated for linearity. The procedures and results are detailed in *Smith et al.* [2012] and *Smith* [2014]. The raw photon counts were collected in the temporal and spatial resolutions of 3 s and 24 m. The USU lidar was operating in two-beam setup, with one pointing 30° off zenith to the north and the other one pointing 20° off zenith to the east. We use the temperatures measured with the eastward beam due to its higher signal-to-noise ratios. For both lidar measurements, temperatures and winds are derived using the raw photon counts smoothed with a 15 min (full width) Hamming window and the window is shifted at a step of ~5 min. Thus, the effective temporal resolution is 7.5 min. The raw photon counts are binned into 0.96 km to retrieve the temperature and winds in order to further increase the precision. Thus, the vertical resolution of both lidar data is 0.96 km. Under such resolutions, the measurement uncertainties in the STAR vertical wind and temperature are ~0.4 m/s and ~0.8 K near the Na layer peak. The temperature uncertainty of the USU lidar near the Na peak is ~1–3 K, and the line-of-sight wind uncertainty is ~1–3 m/s.

The AMTM is an infrared digital imaging system that measures selected emission lines in the mesospheric OH (3,1) band (at ~1.5 μm) to create intensity and temperature maps of the mesosphere around 87 km. The raw temperature data are obtained with a spatial resolution of ~0.5 km and a temporal resolution of ~0.5 min over 120° field of view, with an uncertainty of ±1 K in temperature [*Pautet et al.*, 2014]. Two temperature keograms, one for the south-north (S-N) direction and one for the west-east (W-E), are composed of the S-N and W-E slices cutting across the center of each temperature image and proceeding with time. The horizontal ranges over the S-N and W-E directions are 120 and 150 km, respectively. The AMTM data are also binned into 5 min in order to have the same temporal interval as the lidar data.

3. Identification, Characterization, and Examination of the 1 h Mesoscale Gravity Wave

3.1. Lidar and AMTM Observations Revealing Rich Wave Features

This study was stimulated by the signatures of short-period waves in the vertical winds measured by the STAR Na Doppler lidar at the Table Mountain Lidar Observatory. The most salient wave signatures shown in vertical winds are those with periods of ~30–60 min, persisting almost for the whole night (Figure 1a). The downward phase progressions indicate that the wave signatures are authentic and correspond to upward energy propagation. The signatures of longer-period waves with a period of ~8–10 h are visible in the vertical winds as the background to these short-period waves. Such longer-period waves become the most prominent features in temperatures and horizontal winds, from which higher-frequency waves are more difficult to detect. As will be discussed later, the polarization relation of gravity waves determines that the higher-frequency waves are easier to be detected in vertical winds than in temperatures. Even so, the 1 h waves are noticeable in temperatures measured at Boulder from ~80 to 110 km or even higher (Figure 1b), as well as temperatures and horizontal winds at Logan (Figures 2a–2c), as highlighted by the black arrows.

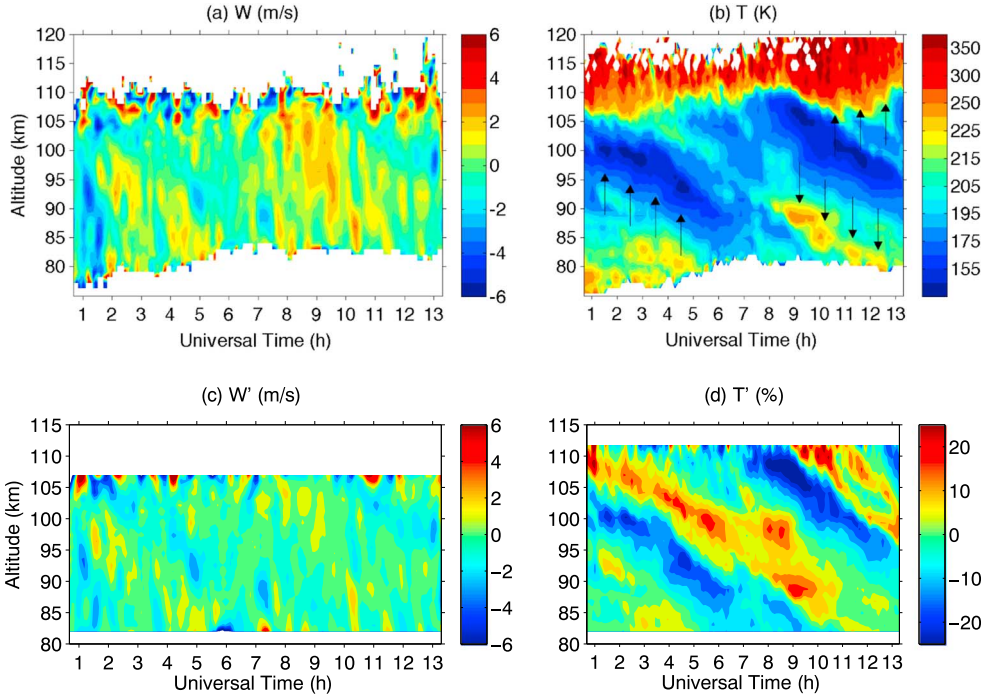

Figure 1. (a) Vertical winds and (b) temperatures measured by the STAR lidar at Boulder, CO, on 27 November 2013. Black arrows are used for illuminating the crests or troughs of the quasi-1 h wave. (c and d) Perturbations of vertical winds and relative temperatures after vertical filtering.

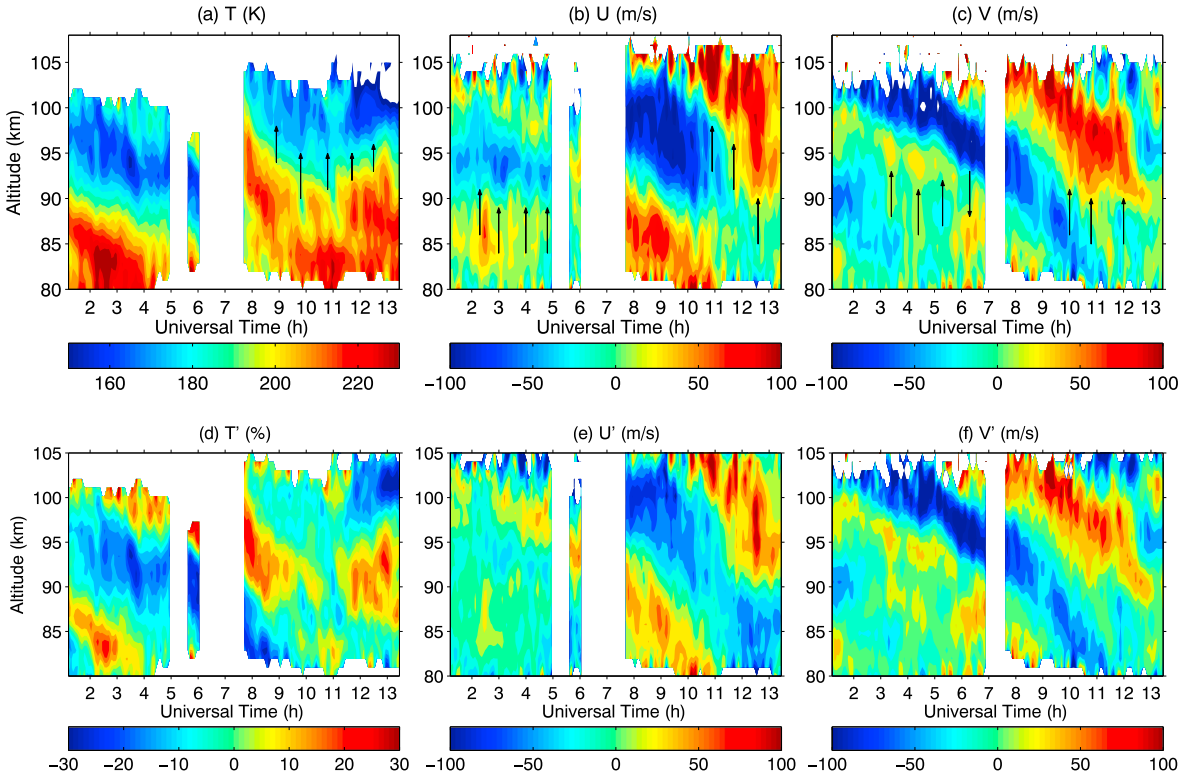

Figure 2. (a) Temperature, (b) zonal wind, and (c) meridional wind measured by the USU Na Doppler lidar at Logan, UT. (d–f) Perturbations after vertical filtering. Blank areas are due to missing data caused by weather.

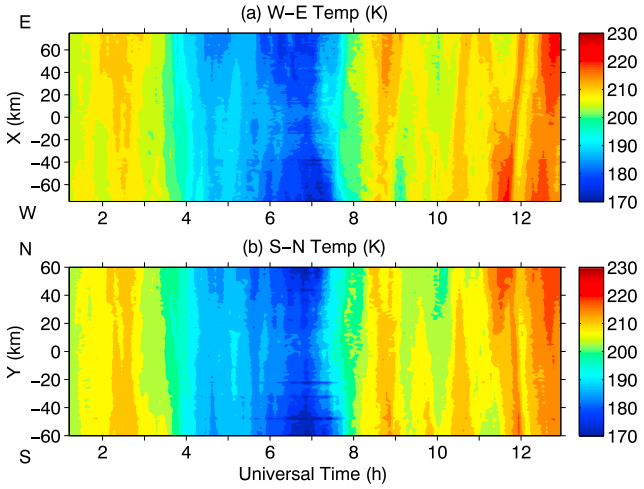

Figure 3. AMTM temperature keograms in the (a) S-N and (b) W-E directions, respectively.

Figure 3 shows the AMTM measurements of OH airglow temperatures at Bear Lake Observatory without any filtering; however, salient GW signatures with a period of ~1 h are visible after ~8 UT in both directions, indicating that the presence of this wave is a robust feature. In addition to this 1 h wave, the longer-period wave signatures are also prominent as shown by cold temperatures between ~4 and 8 UT and two blocks of warm temperatures before and after this period, which is consistent with the USU lidar measurements near 87 km.

To obtain perturbation fields (i.e., u', v', w', and T'/T_0), we subtract the nightly mean at each altitude for the lidar data and at each range for the AMTM. Relative temperature perturbations (T'/T_0) are further derived by dividing with the nightly mean temperatures T_0. For the lidar measurements, we apply a fourth-order Butterworth filter with a passband at 2–60 km with zero paddings in the vertical domain to minimize the contaminations from waves with long vertical wavelengths (λ_z). This vertical filtering is required since the superposition of long waves renders a larger estimation of λ_z than its real value. The resulted wave-induced perturbations are illustrated in Figures 1c, 1d, and 2d–2f for observations at Boulder and Logan, respectively.

Complex wave features are observed in the raw temperatures and vertical and horizontal winds by the lidars and AMTM. Spectral analyses are necessary to identify the dominant wave periods and the time durations with strong wave activities. Since the predominant long-period waves obscure the signatures of the 1 h wave in the regular spectral analysis of temperature field, we introduce the weighted temperature spectrum in the following to highlight the higher-frequency components. The GW nondissipative polarization relation between vertical wind and temperature is written as [e.g., *Vadas*, 2013, equation (B11)]

$$\widetilde{T} = \frac{N^2\left(im + \frac{1}{2H}\right) - \frac{\hat{\omega}^2}{\gamma H}(\gamma - 1)}{g\hat{\omega}\left(-m - \frac{i}{2H} + \frac{i}{\gamma H}\right)}\widetilde{w} \tag{1}$$

where $\widetilde{T}$ and $\widetilde{w}$ are the complex amplitudes including both amplitude and phase information of the relative temperature and vertical wind. m is vertical wave number, and $\hat{\omega}$ is intrinsic frequency of the wave. N and H are the Brunt-Väisälä frequency and the scale height of atmospheric density, respectively. Both of them depend on background temperatures. γ is the ratio of specific heat at constant pressure to that at constant volume. For the 1 h wave, its intrinsic frequency is much smaller than the Brunt-Väisälä frequency (i.e., $\hat{\omega} << N$), and its vertical wavelength satisfies the Boussinesq approximation, i.e., $|\lambda_z| << 4\pi H \approx 90km$. Therefore, equation (1) reduces to

$$\widetilde{T} \approx -\frac{iN^2}{g\hat{\omega}}\widetilde{w} \tag{2}$$

Equation (2) illustrates that for waves with high to medium frequencies, and short vertical wavelengths, the ratio of wave amplitude in vertical wind to relative temperature is nearly proportional to the intrinsic frequency ($\hat{\omega}$). This explains why the 1 h waves can be seen clearly in the vertical winds while longer-period waves are better seen in temperatures (Figures 1a and 1b). In order to delineate the peak frequencies and durations for high-frequency waves in both vertical winds (w') and relative temperatures (T'/T_0), the temperature amplitude spectra are weighted by multiplying the power spectral densities with their corresponding frequencies. Such weighted temperature spectra are not used to quantify any absolute power densities but to enhance the higher-frequency waves.

The normalized wavelet spectra for T'/T_0 after weighting and for w' are illustrated in Figures 4a–4d for Boulder. The waves with periods of ~10–12 h and of ~6–8 h are dominant in both w' and T'/T_0 fields, and

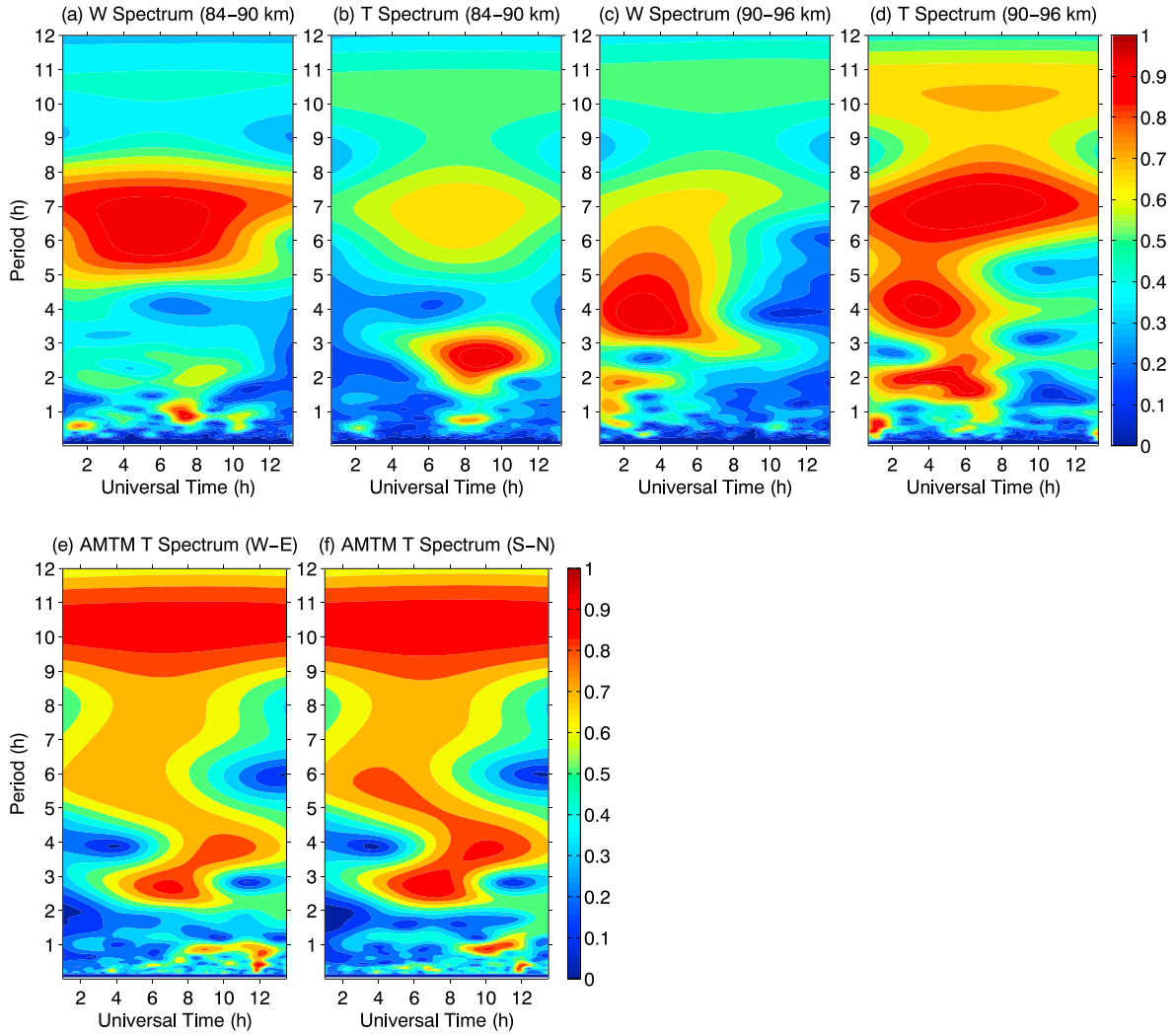

Figure 4. Normalized Morlet wavelet spectra for STAR (a) vertical winds and (b) relative temperatures averaged in 84–90 km, STAR (c) vertical winds and (d) relative temperatures averaged in 90–96 km, and AMTM (e) W-E and (f) S-N relative temperatures, respectively. The relative temperature spectra are weighted by frequency for a better illustration. The data used for the STAR lidar wavelet analyses are the vertically filtered perturbation fields shown in Figures 1c and 1d.

waves with periods varying between 2 and 5 h are also strong. The ~10–12 h wave is likely the semidiurnal tide, considering that both satellite and ground-based observations have revealed that the semidiurnal tides are dominant at the midlatitude of ~40°N [*McLandress et al.*, 1996; *Zhang et al.*, 2006; *Yuan et al.*, 2008], where the observations were made.

In addition to these longer-period waves, the quasi-1 h waves are nonnegligible features in both fields. They tend to be relatively stronger at the intervals of ~2–4, 6–8, and 10–13 UT at Boulder. In the nonweighted temperature spectra (not shown here), strong ~10–12 h and ~6–8 h waves are the most prevalent, and 2–5 h waves are weaker but noticeable, while quasi-1 h wave signatures can be barely seen. The weighted wavelet analyses (not shown) to USU lidar data reveal similar wave features as the STAR lidar results.

Shown in Figures 4e and 4f are the weighted wavelet spectra of AMTM relative temperatures. We found similar dominant wave periods at ~11 and 2–5 h. The 1 h waves are persistently observed in both NS and EW directions and become stronger after ~7.5 UT. Above spectral analyses strongly suggest that the two lidars and the AMTM have observed the same wave fields in the mesopause region, including the quasi 1 h waves. While semidiurnal tides and other longer-period waves have been studied before, this is the first time that such shorter-period waves are observed with two lidars and the AMTM at two separate locations in the Central U.S. Therefore, the current study will focus on the quasi 1 h GWs. This choice is further justified,

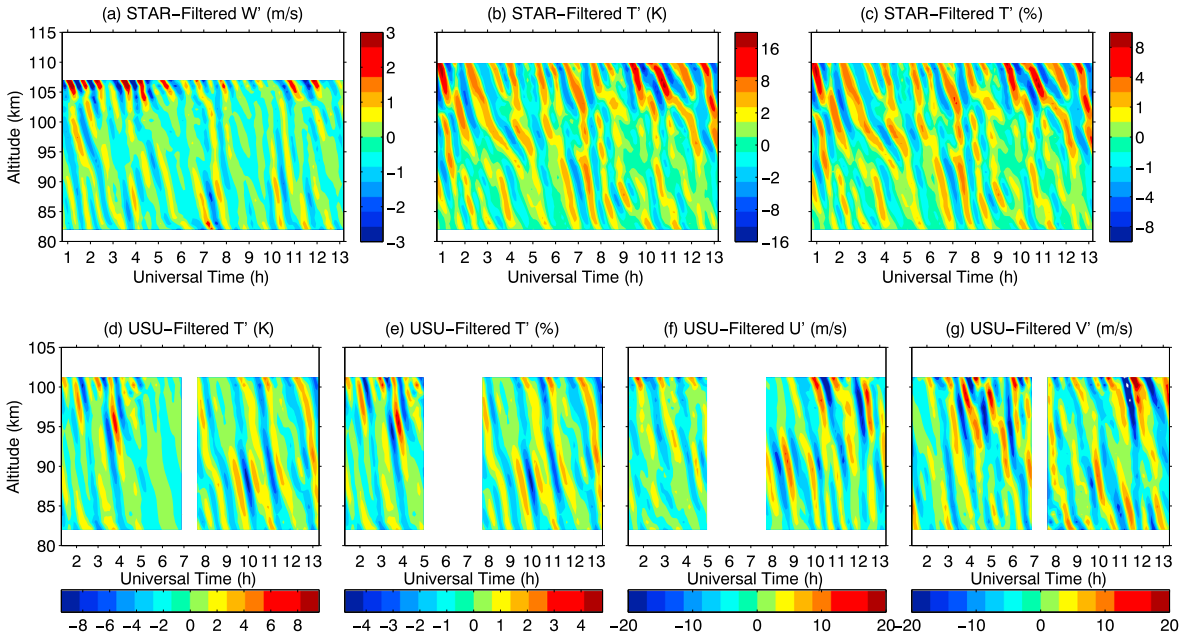

Figure 5. Perturbations after applying a 2DFFT filtering at 0.5–1.5 h in (a) vertical winds, (b) absolute temperatures, (c) relative temperatures at Boulder, and in (d) absolute temperatures, (e) relative temperatures, (f) zonal winds, and (g) meridional winds at Logan, respectively.

as the 1 h waves are indisputable features in STAR raw vertical winds (Figure 1a) and AMTM temperatures (Figures 3). It is also easier with the AMTM data to extract horizontal parameters of a 1 h wave than that of inertial GWs with larger horizontal scales.

3.2. Spectral Filtering to Extract the 1 h Gravity Wave

According to the wavelet spectral analyses, GWs with periods longer than 2 h and shorter than 0.5 h also exist. To extract the 1 h waves, we choose a narrow passband of 0.5–1.5 h to filter out these waves after the vertical filtering. The choice of these cutoff frequencies is a trade-off between minimizing the contaminations from other waves and ensuring the integrity of the desired wave. A 2DFFT (two-dimensional fast Fourier transform) is used to select the desired frequency domain (i.e., 0.5–1.5 h) and to separate the upward and downward propagating waves. Here only the upward propagating waves are considered. The inverse-2DFFT is then applied to reconstruct the perturbation fields in the time and altitude domain, as illustrated in Figure 5. Note that the magnitudes of the 1 h wave above ~105 km in both absolute and relative temperatures increase to relative larger values and we use unequally spaced color bars in Figures 5b and 5c to accommodate the amplitude growth. The 1 h wave signatures are clearly seen at both locations in the temperatures and the three wind components through the altitude range of 82–110 km.

For temperature mapper data, the perturbations are also filtered in both the time and horizontal spatial domains. Similarly to the lidar data, we use the 2DFFT to select the desired frequency band (i.e., 0.5–1.5 h) and the dominant wave propagation directions are determined by inspecting the temperature keograms. The apparent phase progression direction as time proceeds is the dominant direction, which should be from west to east and from north to south (Figure 3). Instead of using a narrowband spatial filtering, all the spectral components for each of the dominant propagation directions are kept. The inverse 2DFFT is then applied to reconstruct the temperature perturbations in the time and spatial domain, which are shown in Figures 6a and 6b. According to a forward modeling test, if waves with similar periods and from two opposite directions are both included, the horizontal wavelength cannot be correctly estimated and is usually biased to a larger number. Therefore, using the 2DFFT method to not only select a frequency band but also keep only one propagation direction against the other is useful and necessary. From the 2-D filtered fields, the cold phases of the quasi-1 h waves in temperature occur near 7, 8, …, 12 UT at −75 km off zenith in the W-E direction and propagate from west to east. The warm phases of the quasi-1 h waves occur near 8, 9, …, 12 UT at −60 km off zenith in the S-N direction and propagate from north to south. Combining these two directions, the 1 h waves should propagate from northwest to southeast. The same patterns and timings can be clearly seen from the unfiltered

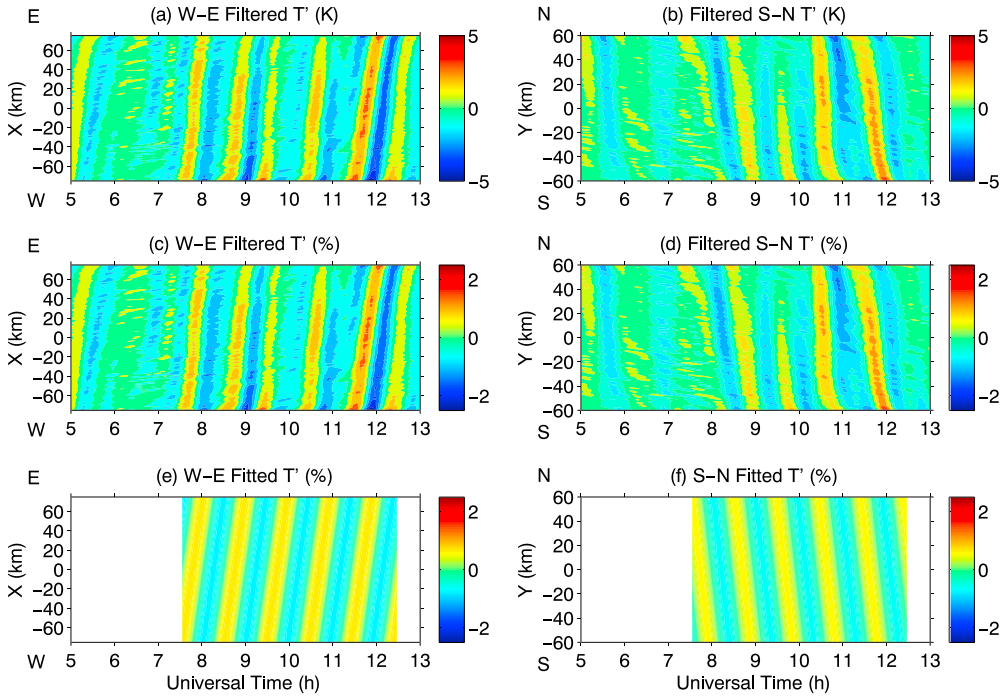

Figure 6. AMTM temperature perturbations filtered at 0.5–1.5 h in the (a) W-E and (b) S-N directions, respectively. (c and d) The same except for the relative temperature perturbations. (e and f) The corresponding 2-D fittings from 7.5 to 12.5 UT using equations (3) and (4) using Figures 6c and 6d.

AMTM data (Figure 3), indicating that the dominant 1 h waves are appropriately extracted. Figure 6 illustrates that the 1 h waves reach their largest amplitudes between ~7.5 and 12.5 UT. This period is selected to derive the horizontal wavelength and propagation direction.

3.3. Horizontal Wavelength and Propagation Direction

The AMTM keograms contain the information of time versus horizontal distance, from which the wave periods and horizontal wavelengths can be inferred from the following 2-D least square fittings:

$$\frac{T'_{WE}(x,t)}{\overline{T}_{WE}(x)} = A_x \cos\left(\frac{2\pi}{\tau_x}t - \frac{2\pi}{\lambda_x}x - \varphi_x\right) \tag{3}$$

$$\frac{T'_{SN}(y,t)}{\overline{T}_{SN}(y)} = A_y \cos\left(\frac{2\pi}{\tau_y}t - \frac{2\pi}{\lambda_y}y - \varphi_y\right) \tag{4}$$

where $T'_{WE}(x,t)/\overline{T}_{WE}(x)$ and $T'_{SN}(x,t)/\overline{T}_{SN}(x)$ are relative temperature perturbations along the W-E and S-N directions (Figures 6a and 6b), respectively. The parameters are optimized by minimizing the root-mean-square of the differences between the original and the fitted data. In addition to wave period (τ_x, τ_y) and vertical wavelength (λ_x, λ_y) in each direction, the fitted parameters also include (A_x, φ_x) and (A_y, φ_y) which are the pairs of wave amplitudes and phases. Wave frequencies are conventionally defined to be positive values; thus, positive λ_x and λ_y denote eastward and northward propagations. The fitted perturbations are

Table 1. Wave Parameters of the 1 h Wave Inferred From the AMTM Measurements

	τ_x (h)	τ_y (h)	λ_x (km)	λ_y (km)	λ_h (km)	c_x[b] (m s^{-1})	c_y[b] (m s^{-1})	c_h[b] (m s^{-1})	θ[c] (deg)
Parameters	0.970	0.967	308	−310	219	88	−89	63	135
Uncertainty[a]	± 0.002	± 0.002	± 6	± 9	± 4	± 2	± 3	± 1	± 1

[a]The uncertainties are standard deviations arising from the 2-D fitting and error propagations.
[b]c_x, c_y, and c_h are the phase speeds of the wave along W-E, S-N, and wave propagation directions, respectively. Negative λ_y and c_y means that the propagation direction is from north to south.
[c]θ is the azimuth angle of the horizontal wave propagation clockwise from north.

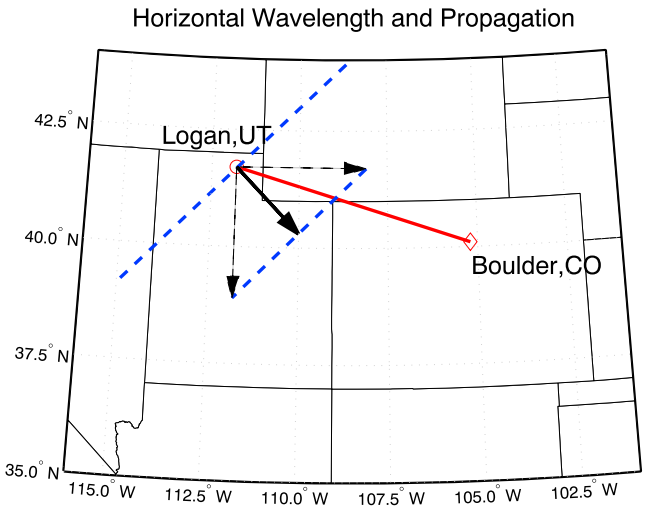

Figure 7. Geographic projection of the horizontal propagation of the 1 h wave on the U.S. map centered at Colorado and Utah. Red line connects Logan and Boulder. Thick black line with an arrow denotes the wave propagation vector (k_h), and its length represents one λ_h. Two dashed blue lines perpendicular to the wave vector denote two consecutive wavefronts.

shown in Figures 6c and 6d, which compare favorably with the fields before fitting (Figures 6a and 6b). The periods in both directions are determined to be 0.97 h, indicating that the same wave is identified. λ_x and λ_y are 308 ± 6 km and -310 ± 9 km, corresponding to phase speeds of 88 ± 2 and -89 ± 3 m/s, respectively (Table 1).

Horizontal wavelength and propagation direction are derived according to the wave number relation, $k_h = \sqrt{k^2 + l^2}$, where $k = 2\pi/\lambda_x$, $l = 2\pi/\lambda_y$, and $k_h = 2\pi/\lambda_h$ represent the wave numbers along W-E, S-N, and the wave propagation direction, respectively. Therefore, the horizontal wavelength of the wave (λ_h) and the azimuth angle of the wave propagation clockwise from north (θ) can be derived from λ_x and λ_y as follows:

$$\lambda_h = \frac{\lambda_x \lambda_y}{\sqrt{\lambda_x^2 + \lambda_y^2}} \tag{5}$$

$$\theta = \tan^{-1}\left(\frac{\lambda_y}{\lambda_x}\right) \tag{6}$$

In this case, the horizontal wavelength is ~219 ± 4 km and the azimuth angle clockwise from north is ~$135° \pm 1$; i.e., the waves propagate southeastward from Logan to Boulder, consistent with the wave propagations determined from Figure 6. The standard deviations of horizontal wavelength and azimuth angle are the uncertainties propagating from λ_x and λ_y.

We project the horizontal structure inferred from the AMTM onto a U.S. map centered on the states of Colorado and Utah, as shown in Figure 7. Under such a scenario, for one cycle of wave propagation, the projection onto the Logan-Boulder line (red line in Figure 7) would be ~244.7 km. Since the distance between these two locations is ~582 km, which is about 2.38 wave cycles, a phase front of the 1 h wave will take ~2.38 h to propagate from Logan to Boulder. In other words, at the same altitudes, the phase shift between the two stations should be $\Delta\varphi = 2\pi(2.38 - 2) \approx 2.39$ rads for the same physical quantity. This estimation is under an assumption that the 1 h wave is homogeneous between the two lidar sites. This assumption could be violated if the background winds and Brunt-Väisälä frequencies (N) at these two locations are very different and lead to the changes in wave parameters and propagation. As will be shown in section 3.5, Boulder and Logan have similar N^2 profiles, which may not cause the obvious inhomogeneity. Because we do not have the range-resolved background winds at Boulder, it is difficult to quantify the effects of the background winds on wave parameters and propagation. But since the observed periods and vertical wavelengths (will be discussed in section 3.4) are compatible at these two locations, the effects of different background winds may be trivial in this case.

3.4. Vertical Wavelength and Amplitude of the 1 h Wave

As mentioned in section 3.1, the intermittency of the 1 h waves is observed in the lidar fields at Boulder. The time periods with strong wave activity are more favorable to derive reliable vertical wavelengths and amplitudes. To identify this time duration for the lidar fields at Logan, we apply a band-pass filter at 0.3–3 h to the perturbation fields (Figures 2d–2f) and then apply the wavelet analyses. The spectra are not weighted here since waves longer than 3 h have been largely removed by the band-pass filter. The wavelet spectra are averaged in the altitude range of 84–96 km and illustrated in Figure 8. Strong 1 h waves are found between 7.7 and 10.7 UT for all the three components at Logan, which are chosen to derive wave amplitudes and phases. Considering that the waves would take ~2.4 h to propagate from Logan to Boulder, we choose the time frame of 10–13 UT for

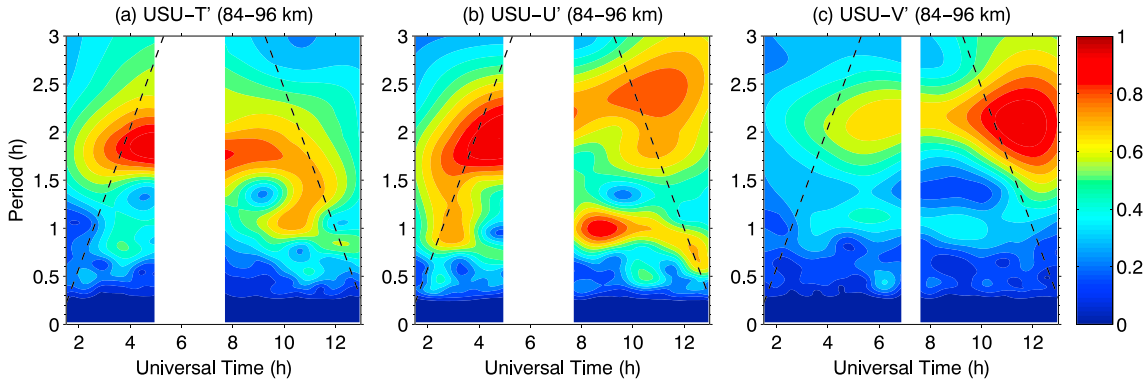

Figure 8. Normalized Morlet wavelet spectra averaged in 84–96 km for USU Na lidar (a) temperature, (b) zonal wind, and (c) meridional wind filtered by a 0.3–3 h band-pass filter. The spectra are normalized after vertical averaging.

Boulder to derive amplitudes and phases, when the 1 h waves also have large amplitudes. These time periods also overlap with the strong 1 h waves showing in the AMTM data.

A sinusoidal function is used to fit the wave amplitude and phase at each altitude based on the filtered perturbation fields (Figure 5), similar to the method used by *Lu et al.* [2009]:

$$y'(z) = a_0(z) + A(z)\cos(\omega t - \varphi(z)) \tag{7}$$

where ω is the wave frequency corresponding to a period of 1 h, close to the vertical mean period and the AMTM results. $A(z)$ and $\varphi(z)$ are the wave amplitudes and phases, respectively, as plotted in Figure 9. The amplitudes vary significantly with altitude, and the mean amplitudes averaged vertically from 82 to 107 km for STAR lidar in relative temperature and vertical wind are 1.0% and 0.44 m/s and for the USU lidar averaged from 84 to 99 km are 1.2%, 6.1, and 5.2 m/s in relative temperature, zonal wind, and meridional winds, respectively (Table 2). The vertical wavelengths are calculated from the vertical gradients of $\varphi(z)$ for these five components, which are close to each other (Table 2), highly suggestive of the same wave source. The mean value of the vertical wavelength is 16.0 ± 0.3 km. The uncertainty of 0.3 km is derived by calculating the error propagation from the uncertainties of the vertical wavelengths in the five components listed in Table 2.

The mean phase difference between Boulder and Logan in relative temperature perturbations (the red solid and dashed lines in Figure 9d) is ~2.0 rads within 84–99 km and ~2.5 rads within 84–90 km where the OH layer measured by the AMTM is centered. Recall that the phase difference derived from the AMTM measurements is around 2.4 rads, which complies well with the lidar observations. Since the three measurements are totally independent, this consistency strongly implies that the same wave is observed at both locations and the wave properties have been properly derived. As the measurements from more than one location are available, diagnosing the phase shift between the different locations is useful to validate whether the horizontal wavelength and azimuth angle have been accurately determined.

3.5. Intrinsic Wave Properties and Examination of Polarization Relations

Since the horizontal and vertical wavelengths of the 1 h wave have been determined by the ground-based observations, the intrinsic wave properties can be diagnosed according to the gravity wave dispersion relation. In addition, the direct observations of the 1 h gravity waves provide quantitative estimations of the wave amplitudes in all the four elementary components (i.e., u', v', w', and T'/T_0). Since such quantifications in the vertical wind have been rare, it is valuable to examine the wave polarization relations by comparing observations with the predictions by the linear wave theory. By using the simultaneous measurements of horizontal winds from a MF radar and temperature from two lidars, *Placke et al.* [2013] have examined the polarization relations between horizontal winds and temperature and found the applicability of the linear wave theory to mesospheric observations after appropriate filtering. The examination of the polarization relations is important for approaches that rely on this assumption. For example, *Ern et al.* [2011] estimate gravity wave momentum fluxes in the mesosphere by assuming the validity of the linear polarization relations.

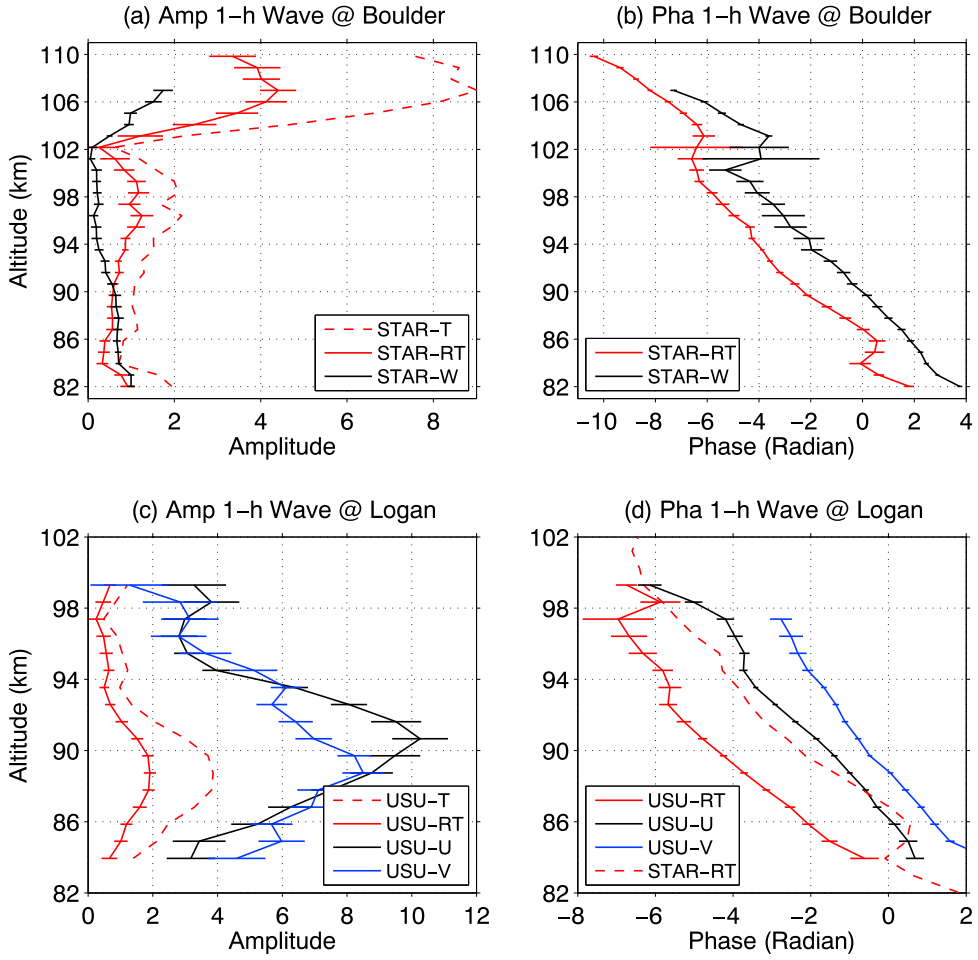

Figure 9. Amplitudes and phases of the 1 h wave in absolute temperature, relative temperature (RT), horizontal wind, and vertical wind. The unit of wave amplitude in absolute temperature is kelvin, in relative temperature is percent, and in winds is m s^{-1}. The phase of the relative temperature at Boulder is also plotted in Figure 9d for a comparison.

The intrinsic frequency whose definition is given by equation (8) can be determined by the dispersion relation for nondissipative gravity waves in equation (9) [e.g., *Fritts and Alexander*, 2003]:

$$\hat{\omega} = \omega - \vec{k} \cdot \vec{U} \tag{8}$$

$$\hat{\omega}^2 = \frac{N^2 k_h^2 + f^2\left(m^2 + \frac{1}{4H^2}\right)}{k_h^2 + m^2 + \frac{1}{4H^2}} \tag{9}$$

where $\hat{\omega}$ and ω are the intrinsic and ground-based frequencies, respectively. $\vec{U}$ is the full mean wind, and $\vec{k} \cdot \vec{U}$ is the mean wind projection along the wave propagation direction $\vec{k}$. The Brunt-Väisälä frequency N and the scale height of atmospheric density H are derived from the lidar-measured background temperatures

Table 2. Vertically Averaged Wave Amplitudes and Vertical Wavelengths for Relative Temperature (RT) and Winds, Obtained From the STAR and USU Lidars

	STAR-RT (%)	STAR-W (m/s)	USU-RT (%)	USU-U (m/s)	USU-V (m/s)
Mean amplitude[a]	1.0	0.44	1.2	6.1	5.2
λ_z (km)	16.2 ± 0.5[b]	15.5 ± 0.7[b]	15.9 ± 0.8[b]	17.4 ± 0.5[b]	14.8 ± 0.4[b]

[a]The mean results are averaged in the vertical ranges of 82–107 and 84–99 km for STAR and USU, respectively.
[b]The uncertainty of the vertical wavelength is estimated from the linear fitting itself without considering the uncertainty of individual data points.

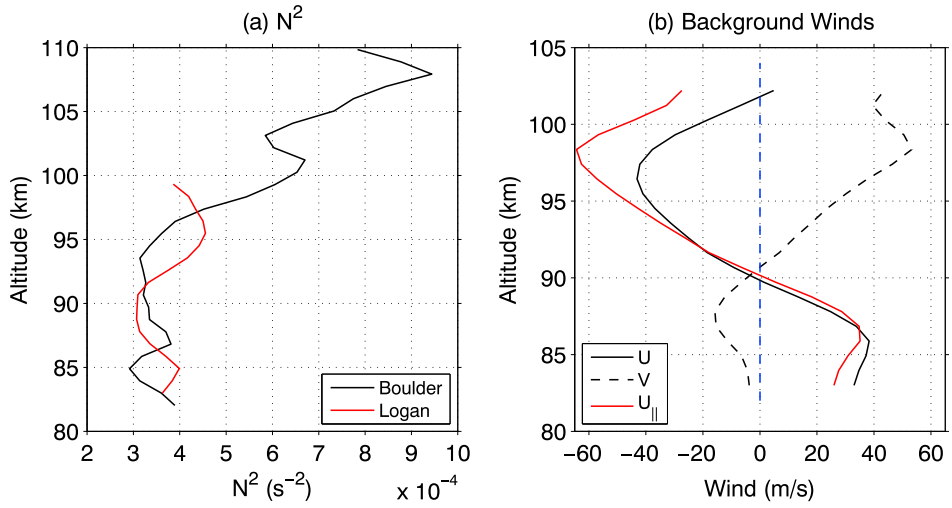

Figure 10. (a) Vertical profiles of N^2 at both Logan and Boulder and (b) zonal (black solid line), meridional (black dashed line), and background wind projecting on the wave propagation direction (red line) averaged from 7.5 to 12.5 UT at Logan, respectively.

using the method in *Lu et al.* [2015]. *Lu et al.* [2015] have shown that the vertical variation of N^2 is significant in the MLT region in Antarctica. The similar large variation of N^2 is observed at Boulder (Figure 10a), which grows from ~3×10^{-4} to $9\times10^{-4}\,s^{-2}$ with altitude increasing from 82 to 110 km. Considering that k_h is derived from the AMTM data, it is necessary to derive weighted N^2, H, and $\vec{U}$ for the OH layer in order to apply them to equations (8) and (9). Because the OH layer intensity has a vertical distribution along the altitude, the range-resolved N^2, H, and $\vec{U}$ measured by lidars are weighted by the OH layer intensity, following the method used in *Zhao et al.* [2005]. As suggested by *Baker and Stair* [1988], we assume a Gaussian distribution of the OH layer with a peak altitude of 87 km and a full width at half maximum of 8.6 km. The weighted N^2 for the OH layer is about $3.4\times10^{-4}\,s^{-2}$, and the weighted H is about 6.0 km. f is the inertial frequency corresponding to a period of 18.7 h at 40°. By substituting these variables into equation (9), the intrinsic frequency is calculated to be ~1.32 h and a mean wind of ~16.6 m/s along the wave direction is required to account for such a Doppler shifting effect. According to the horizontal winds measured by the USU lidar during 7.5 and 12.5 UT (Figure 10b), the projection of the weighted mean wind on the wave propagation direction within the OH layer is about ~17 m/s, which matches the estimation from the dispersion relation and implies that the intrinsic property of the 1 h wave has been correctly derived.

The intrinsic horizontal and vertical group velocities describe the energy propagation of the wave packet against the mean wind. They are defined as the partial derivatives of intrinsic frequency with respect to wave numbers, which are inherently correlated with each other via the dispersion relation. By taking the partial derivatives of equation (9) to k_h and m, the intrinsic group velocities are derived as [e.g., *Fritts and Alexander*, 2003; *Chen et al.*, 2013]

$$\hat{c}_{gh} = \frac{\partial\hat{\omega}}{\partial k_h} = \frac{k_h\left(N^2-\hat{\omega}^2\right)}{\hat{\omega}\left(k_h^2+m^2+\frac{1}{4H^2}\right)} \tag{10}$$

$$\hat{c}_{gz} = \frac{\partial\hat{\omega}}{\partial m} = -\frac{m\left(\hat{\omega}^2-f^2\right)}{\hat{\omega}\left(k_h^2+m^2+\frac{1}{4H^2}\right)} \tag{11}$$

By substituting all the variables derived and defined previously, we have $\hat{c}_{gh}$ and $\hat{c}_{gz}$ equal to ~45.5 and 3.2 m/s, respectively. For the ground-based group velocities, they are the same in the vertical direction assuming that the mean vertical wind approaches zero, while in the horizontal plane, the ground-based group velocity should be $c_{gh}=\hat{c}_{gh}+\bar{u}$ and equals to ~62.1 m/s. Therefore, the elevation angle of the wave packet is about 3.0°.

The polarization relation between relative temperature and vertical wind has been given in equation (1) for non-dissipative gravity waves, which will be examined using the STAR lidar measurements. The relative temperature,

Table 3. Amplitude (A) Ratios and Phase (φ) Differences of $\widetilde{u}, \widetilde{v}, \widetilde{w}$, and $\widetilde{T}$ Observed by the STAR and USU Lidars Versus the Predictions by the Linear Wave Theory

	$A(\widetilde{T})/A(\widetilde{w})$ (%/(m/s))	$\varphi(\widetilde{T})-\varphi(\widetilde{w})$ (rad)	$A(\widetilde{T})/A(\widetilde{u})$ (%/(m/s))	$\varphi(\widetilde{T})-\varphi(\widetilde{u})$ (rad)	$A(\widetilde{u})/A(\widetilde{v})$ (−)	$\varphi(\widetilde{u})-\varphi(\widetilde{v})$ (rad)
PREs[a]	2.8	−1.5	0.27	−1.3	1.0	3.0
OBVs[a]	3.2[b] ± 1.8[c]	−1.9[b] ± 0.5[c]	0.20[b] ± 0.07[c]	−2.8[b] ± 0.4[c]	1.2[b] ± 0.5[c]	2.8[b] ± 0.3[c]

[a]PREs denotes predictions by the linear wave theory and OBVs denotes observations.
[b]The mean results are obtained by performing the average in the vertical range of 82–107 and of 84–99 km for the STAR and USU lidar data, respectively.
[c]The uncertainties represent the standard deviations of the amplitude ratios and phase differences.

zonal, and meridional winds measured by the USU lidar should obey the following compressible and nondissipative polarization relations according to the linear wave theory [e.g., *Fritts and Alexander*, 2003; *Vadas*, 2013]:

$$\widetilde{T}=\frac{N^2\left(im+\frac{1}{2H}\right)-\frac{\hat{\omega}^2}{\gamma H}(\gamma-1)}{g}\frac{\left(\hat{\omega}^2-f^2\right)(k\hat{\omega}-ifl)}{\left(N^2-\hat{\omega}^2\right)\left(k^2\hat{\omega}^2+f^2l^2\right)}\widetilde{u} \tag{12}$$

$$\widetilde{u}=\frac{(i\hat{\omega}k-fl)}{(i\hat{\omega}l+fk)}\widetilde{v} \tag{13}$$

where $\widetilde{T}, \widetilde{w}, \widetilde{u}$, and $\widetilde{v}$ are the complex amplitudes of relative temperature, vertical, zonal, and meridional winds, respectively. The definitions of other variables can be found in the previous equations. Equation (13) is derived based on equations (B8) and (B11) in *Vadas* [2013] but with i being replaced by $-i$ due to the different definitions of waveforms. We calculate the ratios of the complex amplitudes of $\widetilde{T}/\widetilde{w}$, $\widetilde{T}/\widetilde{u}$, and $\widetilde{u}/\widetilde{v}$ predicted by the theory, with their absolute values representing the real amplitude ratios (denoted by $A\left(\widetilde{T}\right)/A(\widetilde{w}), A\left(\widetilde{T}\right)/A(\widetilde{u})$, and $A(\widetilde{u})/A(\widetilde{v})$) and the imaginary parts corresponding to the phase differences (denoted by $\varphi\left(\widetilde{T}\right)-\varphi(\widetilde{w}), \varphi\left(\widetilde{T}\right)-\varphi(\widetilde{u})$, and $\varphi(\widetilde{u})-\varphi(\widetilde{v})$). It should be noted that for estimating the phase differences from the observations, it is assumed that the complex amplitudes of the parameters considered have the same inherent phase. From observations, these quantities are calculated at each altitude using the results in Figure 9. Their vertical means averaged from 82 to 107 km for the STAR lidar and from 84 to 99 km for the USU lidar and the standard derivations are computed to represent their distributions. Due to the beam settings of the USU lidar, the horizontal distance between the east and north beams ranges from 55 to 68 km in the MLT region, which can consist of approximately one fourth wave cycle. The phase difference between $\widetilde{u}$ and $\widetilde{v}$ is adjusted to compensate such an effect at 90 km. The comparisons between observations and the theoretical predictions are listed in Table 3.

The mean values of the observations are slightly different from the theoretical predictions, which are expected and may be indicative of the effects from wave dissipations that can modify the polarization relations [*Vadas and Nicolls*, 2012; *Nicolls et al.*, 2012]. The nonnegligible standard deviations indicate that the polarization relation varies with altitude and the wave behaves differently at different regions in the complex atmosphere. Although the discrepancies are noticed, the predicted polarization relations are generally within the range of the observed values except that the predicted phase difference of −1.3 between $\widetilde{T}$ and $\widetilde{u}$ is outside of the observational range, i.e., -2.8 ± 0.4. It should be mentioned that a phase correction due to different beam locations is not required for the phase difference between $\widetilde{T}$ and $\widetilde{u}$ because $\widetilde{T}$ is derived from the eastward beam of the USU lidar.

4. Conclusions

Using simultaneous observations of two Na Doppler lidars of CRRL and a temperature mapper, we perform a coordinated study of a 1 h mesoscale wave event occurring in the night of 27 November 2013 over the Central US. The horizontal wavelength of this wave is ~219 km in the MLT region, corresponding to a phase speed of 63 m/s. It propagates southeastward from Logan, UT, to Boulder, CO, with an azimuth angle of ~135°. The vertical wavelength is ~16 km determined from the lidar measurements. The downward phase progression indicates upward energy propagation in the MLT region and implies a wave source from below. The horizontal and vertical group velocities are ~62.1 and 3.2 m/s, respectively, corresponding to an elevation angle of 3.0° from the horizon. The intrinsic period of the wave is determined to be ~1.32 h around the OH airglow layer and Doppler shifted by a mean wind of ~17 m/s.

The simultaneous and direct quantifications of the wave amplitudes and phases in all the four elementary components (i.e., u', v', w', and T'/T_0) have been provided for the 1 h wave over Logan and Boulder, which enable the examination of the wave polarization relations. Although the observed amplitude ratios between $\widetilde{T}$ and $\widetilde{w}$, $\widetilde{T}$ and $\widetilde{u}$, and $\vec{u}$ and $\vec{v}$ contain the predicted values from the linear wave theory, these observed ratios vary substantially with altitude and show some discrepancies from the theoretical predictions for nondissipative waves. The observed phase differences between $\widetilde{T}$ and $\widetilde{w}$ and between $\widetilde{u}$ and $\widetilde{v}$ overlap theoretical values; however, the observed phase difference between $\widetilde{T}$ and $\widetilde{u}$ is much larger than the corresponding theoretical value. These discrepancies may result from the dissipative nature of the 1 h waves, which modify the wave polarization relations.

The vertically range resolved lidars can provide the vertical structure of the wave, while the temperature mapper and airglows can be used to delineate the horizontal structure. This study illustrates a great capability of combining these two techniques to fully characterize mesoscale gravity waves. The observations from multiple stations and the phase shifts between them are very useful to validate the information of horizontal wave wavelength and propagation direction. A preliminary inspection of the Na lidar data at Boulder, CO, has shown a frequent occurrence of the 0.5–2 h wave signatures in vertical wind, temperature, and Na density variations in the wintertime, when the strong tropospheric upper level jet can persistently generate mesoscale gravity waves [*Zhang*, 2004; *Plougonven and Zhang*, 2014]. Still, other wave sources cannot be excluded. Although the weather should be clear locally at Boulder and Logan in order to operate lidars and temperature mapper, the 1 h wave can still be possibly generated by a remote convection activity, considering that the horizontal scale of the 1 h wave is large enough to have been propagating far away from the convective source [*Alexander and Holton*, 1997]. Observational evidences have shown that convectively generated gravity waves can travel considerable distances before reaching the MLT region [*Wrasse et al.*, 2006; *Ern et al.*, 2013]. A statistical study of their characteristics is needed to fully understand how often and to what magnitudes these high- and medium-frequency GWs occur in the MLT region and whether they will modulate the upper atmosphere variability. The current study has developed a systematic method to diagnose the 0.5–2 h waves using multiple data sources and various analysis methods, which will be employed in the future to link the observed MLT waves with the possible wave sources in the lower atmosphere and with the wave-induced ionospheric variability such as medium-scale TIDs.

Acknowledgments

The STAR lidar work was supported by NSF CRRL grant AGS-1136272. Xian Lu's research was partially supported by the NSF CEDAR grant AGS-1343106 and Cao Chen's by NSF grant PLR-1246405. John A. Smith sincerely acknowledges the generous support of the NASA Earth and Space Science Fellowship (NESSF) with NASA grant NNX09AO35H and of the CIRES Graduate Student Research Fellowship (GSRF). The USU lidar study was performed as a part of the collaborative research program supported by NSF CRRL grant AGS-1135882. The USU AMTM was designed under the Air Force DURIP grant F49620-02-1-0258 and operated through the NSF grant 1042227. We thank Ian F. Barry and Muzhou Lu for helping on the language editing. The data producing the results of this paper can be requested from the corresponding authors (xian.lu@colorado.edu and xinzhao.chu@colorado.edu).

References

Alexander, M. J. (1998), Interpretations of observed climatological patterns in stratospheric gravity wave variance, *J. Geophys. Res.*, *103*(D8), 8627–8640, doi:10.1029/97JD03325.

Alexander, M. J., and C. Barnet (2007), Using satellite observations to constrain gravity wave parameterizations for global models, *J. Atmos. Sci.*, *64*(5), 1652–1665.

Alexander, M. J., and J. R. Holton (1997), A model study of zonal forcing in the equatorial stratosphere by convectively induced gravity waves, *J. Atmos. Sci.*, *54*, 408–419.

Baker, D. J., and J. A. T. Stair (1988), Rocket measurements of the altitude distributions of the hydroxyl airglow, *Phys. Scr.*, *37*, 611–622, doi:10.1088/0031-8949/37/4/021.

Beatty, T. J., C. A. Hostetler, and C. S. Gardner (1992), Lidar observations of gravity waves and their spectra near the mesopause and stratopause at Arecibo, *J. Atmos. Sci.*, *49*, 477–496.

Bertin, F., J. Testud, L. Kersley, and P. R. Rees (1978), The meteorological jet stream as a source of medium scale gravity waves in the thermosphere: An experimental study, *J. Atmos. Terr. Phys.*, *40*, 1161–1183, doi:10.1016/0021-9169(78)90067-3.

Cai, X., T. Yuan, Y. Zhao, P.-D. Pautet, M. J. Taylor, and W. R. Pendleton Jr. (2014), A coordinated investigation of the gravity wave breaking and the associated dynamical instability by a Na lidar and an Advanced Mesosphere Temperature Mapper over Logan, UT (41.7°N, 111.8°W), *J. Geophys. Res. Space Physics*, *119*, 6852–6864, doi:10.1002/2014JA020131.

Chen, C., X. Chu, A. J. McDonald, S. L. Vadas, Z. Yu, W. Fong, and X. Lu (2013), Inertia-gravity waves in Antarctica: A case study using simultaneous lidar and radar measurements at McMurdo/Scott Base (77.8°S, 166.7°E), *J. Geophys. Res. Atmos.*, *118*, 2794–2808, doi:10.1002/jgrd.50318.

Ding, F., W. Wan, G. Xu, T. Yu, G. Yang, and J. Wang (2011), Climatology of medium-scale traveling ionospheric disturbances observed by a GPS network in central China, *J. Geophys. Res.*, *116*, A09327, doi:10.1029/2011JA016545.

Ern, M., P. Preusse, J. C. Gille, C. L. Hepplewhite, M. G. Mlynczak, J. M. Russell III, and M. Riese (2011), Implications for atmospheric dynamics derived from global observations of gravity wave momentum flux in stratosphere and mesosphere, *J. Geophys. Res.*, *116*, D19107, doi:10.1029/2011JD015821.

Ern, M., P. Preusse, S. Kalisch, M. Kaufmann, and M. Riese (2013), Role of gravity waves in the forcing of quasi two-day waves in the mesosphere: An observational study, *J. Geophys. Res. Atmos.*, *118*, 3467–3485, doi:10.1029/2012JD018208.

Franke, S. J., T. Beatty, D. Thorsen, C. H. Liu, C. S. Gardner, F. L. Roesler, and J. Harlander (1990), Simultaneous Na lidar and HF radar observations of vertical velocities in the mesosphere above Urbana, IL, *Geophys. Res. Lett.*, *17*, 69–72, doi:10.1029/GL017i001p00069.

Fritts, D. C., and M. J. Alexander (2003), Gravity wave dynamics and effects in the middle atmosphere, *Rev. Geophys.*, *41*(1), 1003, doi:10.1029/2001RG000106.

Fritts, D. C., and G. D. Nastrom (1992), Sources of mesoscale variability of gravity waves. Part II: Frontal, convective, and jet stream excitation, *J. Atmos. Sci.*, *49*, 111–127.

Fritts, D. C., P.-D. Pautet, K. Bossert, M. J. Taylor, B. P. Williams, H. Iimura, T. Yuan, N. J. Mitchell, and G. Stober (2014), Quantifying gravity wave momentum fluxes with Mesosphere Temperature Mappers and correlative instrumentation, *J. Geophys. Res. Atmos.*, *119*, 13,583–13,603, doi:10.1002/2014JD022150.

Garcia, R. R., and S. Solomon (1985), The effect of breaking gravity waves on the dynamics and chemical composition of the mesosphere and lower thermosphere, *J. Geophys. Res.*, *90*(D2), 3850–3868, doi:10.1029/JD090iD02p03850.

Gardner, C. S., and A. Z. Liu (2007), Seasonal variations of the vertical fluxes of heat and horizontal momentum in the mesopause region at Starfire Optical Range, New Mexico, *J. Geophys. Res.*, *112*, D09113, doi:10.1029/2005JD006179.

Gardner, C. S., and A. Z. Liu (2010), Wave-induced transport of atmospheric constituents and its effect on the mesospheric Na layer, *J. Geophys. Res.*, *115*, D20302, doi:10.1029/2010JD014140.

Gardner, C. S., and M. J. Taylor (1998), Observational limits for lidar, radar, and airglow imager measurements of gravity wave parameters, *J. Geophys. Res.*, *103*(D6), 6427–6437, doi:10.1029/97JD03378.

Gardner, C. S., and W. Yang (1998), Measurements of the dynamical cooling rate associated with the vertical transport of heat by dissipating gravity waves in the mesopause region at the Starfire Optical Range, New Mexico, *J. Geophys. Res.*, *103*, 16,909–16,926, doi:10.1029/98JD00683.

Gardner, C. S., M. S. Miller, and C. H. Liu (1989), Rayleigh lidar observations of gravity wave activity in the upper stratosphere at Urbana, Illinois, *J. Atmos. Sci.*, *46*(12), 1838–1854, doi:10.1175/1520-0469(1989)046<1838:RLOOGW>2.0.CO;2.

Gardner, C. S., X. Tao, and G. C. Papen (1995), Simultaneous lidar observations of vertical wind, temperature and density profiles in the upper mesosphere: Evidence for nonseparability of atmospheric perturbation spectra, *Geophys. Res. Lett.*, *22*(20), 2877–2880, doi:10.1029/95GL02783.

Holton, J. R. (1983), The influence of gravity wave breaking on the circulation of the middle atmosphere, *J. Atmos. Sci.*, *40*, 2497–2507.

Hooke, W. H. (1986), Gravity waves, in *Mesoscale Meteorology and Forecasting*, edited by P. S. Ray, pp. 272–278, Am. Meteorol. Soc., Boston, Mass.

Hoppe, U.-P., and D. C. Fritts (1995), High-resolution measurements of vertical velocity with the EISCAT VHF radar: 1. Motion field characteristics and measurement biases, *J. Geophys. Res.*, *100*, 16,813–16,826, doi:10.1029/95JD01466.

Hu, X., A. Z. Liu, C. S. Gardner, and G. R. Swenson (2002), Characteristics of quasi-monochromatic gravity waves observed with Na lidar in the mesopause region at Starfire Optical Range, NM, *Geophys. Res. Lett.*, *29*(24), 2169, doi:10.1029/2002GL014975.

Huang, W., X. Chu, C. S. Gardner, Z. Wang, W. Fong, J. A. Smith, and B. R. Roberts (2013), Simultaneous, common-volume lidar observations and theoretical studies of correlations among Fe/Na layers and temperatures in the mesosphere and lower thermosphere at Boulder Table Mountain (40°N, 105°W), Colorado, *J. Geophys. Res. Atmos.*, *118*, 8748–8759, doi:10.1002/jgrd.50670.

Koch, S., and C. O'Handly (1997), Operational forecasting and detection of mesoscale gravity waves, *Weather Forecasting*, *12*, 253–281.

Kubota, M., M. Conde, M. Ishii, Y. Murayama, and H. Jin (2011), Characteristics of nighttime medium-scale traveling ionospheric disturbances observed over Alaska, *J. Geophys. Res.*, *116*, A05307, doi:10.1029/2010JA016212.

Li, Z., A. Z. Liu, X. Lu, G. R. Swenson, and S. J. Franke (2011), Gravity wave characteristics from OH airglow imager over Maui, *J. Geophys. Res.*, *116*, D22115, doi:10.1029/2011JD015870.

Liu, A. Z., and C. S. Gardner (2005), Vertical heat and constituent transport in the mesopause region by dissipating gravity waves at Maui, Hawaii (20.7°N), and Starfire Optical Range, New Mexico (35°N), *J. Geophys. Res.*, *110*, D09S13, doi:10.1029/2004JD004965.

Lu, X., A. Z. Liu, G. R. Swenson, T. Li, T. Leblanc, and I. S. McDermid (2009), Gravity wave propagation and dissipation from the stratosphere to the lower thermosphere, *J. Geophys. Res.*, *114*, D11101, doi:10.1029/2008JD010112.

Lu, X., X. Chu, W. Fong, C. Chen, Z. Yu, B. R. Roberts, and A. J. McDonald (2015), Vertical evolution of potential energy density and vertical wave number spectrum of Antarctic gravity waves from 35 to 105 km at McMurdo (77.8°S, 166.7°E), *J. Geophys. Res. Atmos.*, *120*, 2719–2737, doi:10.1002/2014JD022751.

McDonald, A. J. (2012), Gravity wave occurrence statistics derived from paired COSMIC/FORMOSAT3 observations, *J. Geophys. Res.*, *117*, D15106, doi:10.1029/2011JD016715.

McDonald, A. J., B. Tan, and X. Chu (2010), Role of gravity waves in the spatial and temporal variability of stratospheric temperature measured by COSMIC/FORMOSAT3 and Rayleigh lidar observations, *J. Geophys. Res.*, *115*, D19128, doi:10.1029/2009JD013658.

McLandress, C., G. G. Shepherd, and B. H. Solheim (1996), Satellite observations of thermospheric tides: Results from the wind imaging interferometer on UARS, *J. Geophys. Res.*, *101*, 4093–4114, doi:10.1029/95JD03359.

Mitchell, N. J., and V. S. C. Howells (1998), Vertical velocities associated with gravity waves measured in the mesosphere and lower thermosphere with the EISCAT VHF radar, *Ann. Geophys.*, *16*, 1367–1379.

Nicolls, M. J., S. L. Vadas, J. W. Meriwether, M. G. Conde, and D. Hampton (2012), The phases and amplitudes of gravity waves propagating and dissipating in the thermosphere: Application to measurements over Alaska, *J. Geophys. Res.*, *117*, A05323, doi:10.1029/2012JA017542.

Pautet, P.-D., M. J. Taylor, A. Z. Liu, and G. R. Swenson (2005), Climatology of short-period gravity waves observed over northern Australia during the Darwin Area Wave Experiment (DAWEX) and their dominant source regions, *J. Geophys. Res.*, *110*, D03S90, doi:10.1029/2004JD004954.

Pautet, P.-D., M. J. Taylor, Y. Zhao, T. Yuan, W. R. Pendleton Jr., R. Esplin, and D. McLain (2014), An advanced mesospheric temperature mapper for high-latitude airglow studies, *Appl. Opt.*, *53*(26), 5934–5943.

Placke, M., P. Hoffmann, M. Gerding, E. Becker, and M. Rapp (2013), Testing linear gravity wave theory with simultaneous wind and temperature data from the mesosphere, *J. Atmos. Sol. Terr. Phys.*, *93*, 57–69, doi:10.1016/j.jastp.2012.11.012.

Plougonven, R., and F. Zhang (2014), Internal gravity waves from atmospheric jets and fronts, *Rev. Geophys.*, *52*, 33–76, doi:10.1002/2012RG000419.

Preusse, P., S. D. Eckermann, and M. Ern (2008), Transparency of the atmosphere to short horizontal wavelength gravity waves, *J. Geophys. Res.*, *113*, D24104, doi:10.1029/2007JD009682.

Sato, K. (1994), A statistical study of the structure, saturation and sources of inertio-gravity waves in the lower stratosphere observed with the MU radar, *J. Atmos. Terr. Phys.*, *56*(6), 755–774, doi:10.1016/0021-9169(94)90131-7.

Sato, K., and M. Yoshiki (2008), Gravity wave generation around the polar vortex in the stratosphere revealed by 3 hourly radiosonde observations at Syowa Station, *J. Atmos. Sci.*, *65*, 3719–3735, doi:10.1175/2008JAS2539.1.

She, C. Y., and D. A. Krueger (2007), Laser-induced fluorescence: Spectroscopy in the sky, *Opt. Photonics News*, *18*, 35–41.

Shiokawa, K., S. Suzuki, Y. Otsuka, T. Ogawa, T. Nakamura, and T. Horinouchi (2007), An intense gravity wave near the mesopause region observed by a Fabry-Perot interferometer and an airglow imager, *J. Geophys. Res.*, *112*, D07106, doi:10.1029/2006JD007385.

Smith, J. (2014), Exploration of a whole atmosphere lidar concept for whole atmosphere science: Advances in resonance Doppler lidar technologies, PhD thesis, p. 23, Univ. of Colo. Boulder, 26 Nov.

Smith, J. A., and X. Chu (2015), High-efficiency receiver architecture for resonance-fluorescence and Doppler lidars, *Appl. Opt.*, *54*(11), 3173–3184, doi:10.1364/AO.54.003173.

Smith, J. A., W. Fong, B. Roberts, W. Huang, and X. Chu (2012), Very high-resolution Na Doppler LIDAR at Boulder, Colorado, in *Proceeding of the 26th International Laser Radar Conference*, pp. 151–154, Porto Heli, Greece, 25–29 June.

Suzuki, S., F.-J. Lübken, G. Baumgarten, N. Kaifler, R. Eixmann, B. P. Williams, and T. Nakamura (2013), Vertical propagation of a mesoscale gravity wave from the lower to the upper atmosphere, *J. Atmos. Sol. Terr. Phys.*, *97*, 29–36.

Uccellini, L. W., and S. E. Koch (1987), The synoptic setting and possible energy sources for mesoscale wave disturbances, *Mon. Weather Rev.*, *115*, 721–729.

Vadas, S. L. (2013), Compressible f-plane solutions to body forces, heatings, and coolings, and application to the primary and secondary gravity waves generated by a deep convective plume, *J. Geophys. Res. Space Physics*, *118*, 2377–2397, doi:10.1002/jgra.50163.

Vadas, S. L., and M. J. Nicolls (2012), The phases and amplitudes of gravity waves propagating and dissipating in the thermosphere: Theory, *J. Geophys. Res.*, *117*, A05322, doi:10.1029/2011JA017426.

Vincent, R. A., and M. J. Alexander (2000), Gravity waves in the tropical lower stratosphere: An observational study of seasonal and interannual variability, *J. Geophys. Res.*, *105*, 17,971–17,982, doi:10.1029/2000JD900196.

Wrasse, C. M., et al. (2006), Mesospheric gravity waves observed near equatorial and low-middle latitude stations: Wave characteristics and reverse ray tracing results, *Ann. Geophys.*, *24*, 3229–3240, doi:10.5194/angeo-24-3229-2006.

Yuan, T., H. Schmidt, C. Y. She, D. A. Krueger, and S. Reising (2008), Seasonal variations of semidiurnal tidal perturbations in mesopause region temperature and zonal and meridional winds above Fort Collins, Colorado (40.6°N, 105.1°W), *J. Geophys. Res.*, *113*, D20103, doi:10.1029/2007JD009687.

Yuan, T., C. Fish, J. Sojka, D. Rice, M. J. Taylor, and N. J. Mitchell (2013), Coordinated investigation of summer time mid-latitude descending E layer (Es) perturbations using Na lidar, ionosonde, and meteor wind radar observations over Logan, Utah (41.7°N, 111.8°W), *J. Geophys. Res. Atmos.*, *118*, 1734–1746, doi:10.1029/2012JD017845.

Yuan, T., P.-D. Pautet, Y. Zhao, X. Cai, N. R. Criddle, M. J. Taylor, and W. R. Pendleton Jr. (2014), Coordinated investigation of mid-latitude upper mesospheric temperature inversion layers and the associated gravity wave forcing by Na lidar and Advanced Mesospheric Temperature Mapper in Logan, Utah, *J. Geophys. Res. Atmos.*, *119*, 3756–3769, doi:10.1002/2013JD020586.

Zhang, F. (2004), Generation of mesoscale gravity waves in the upper-tropospheric jet-front systems, *J. Atmos. Sci.*, *61*, 440–457.

Zhang, X., J. M. Forbes, M. E. Hagan, J. M. Russell III, S. E. Palo, C. J. Mertens, and M. G. Mlynczak (2006), Monthly tidal temperatures 20–120 km from TIMED/SABER, *J. Geophys. Res.*, *111*, A10S08, doi:10.1029/2005JA011504.

Zhao, Y., M. J. Taylor, and X. Chu (2005), Comparison of simultaneous Na lidar and mesospheric nightglow temperature measurements and the effects of tides on the emission layer heights, *J. Geophys. Res.*, *110*, D09S07, doi:10.1029/2004JD005115.